On-surface Synthesis of [7]triangulene Quantum Ring *via* Antidot Engineering

Jie Su[†][a], Wei Fan[†][a], Pingo Mutombo[†][c], Xinnan Peng[a], Shaotang Song[a], Mykola Telychko[a], Pavel Jelínek[*][c,d], Jishan Wu[*][a] and Jiong Lu[*][a,b]

[a]Department of Chemistry, National University of Singapore, 3 Science Drive 3, Singapore 117543, Singapore.

[b]Centre for Advanced 2D Materials (CA2DM), National University of Singapore, 6 Science Drive 2, Singapore 117546, Singapore.

[c]Institute of Physics, The Czech Academy of Sciences, Prague 16200, Czech Republic.

[d]Regional Centre of Advanced Technologies and Materials, Palacký University, Olomouc 78371, Czech Republic.

[†]These authors contributed equally to this work

[*] Corresponding authors. Email: jelinekp@fzu.cz (P. Jelínek); chmwuj@nus.edu.sg (J. Wu); chmluj@nus.edu.sg (J. Lu)

Abstract: The ability to engineer geometrically well-defined antidots in large triangulene homologues allows for creating an entire family of triangulene quantum ring (TQR) structures with tunable high-spin ground state and magnetic ordering, crucial for next-generation molecular spintronic devices. Herein, we report the synthesis of an open-shell [7]triangulene quantum ring ([7]TQR) molecule on Au(111) through the surface-assisted cyclodehydrogenation of a rationally-designed kekulene derivative. Bond-resolved scanning tunneling microscopy (BR-STM) unambiguously imaged the molecular backbone of a single [7]TQR with a triangular zigzag edge topology, which can be viewed as [7]triangulene decorated with a coronene-like antidot in the molecular centre. Additionally, dI/dV mapping reveals that both inner and outer zigzag edges contribute to the edge-localized and spin-polarized electronic states of [7]TQR. Both experimental results and spin-polarized density functional theory calculations indicate that [7]TQR

retains its open-shell septuple ground-state ($S = 3$) on Au(111). This work demonstrates a new route for the design of high-spin graphene quantum rings as the key components for future quantum devices.

Introduction

Open-shell graphene nanostructures (GNs) have attracted tremendous interest due to their unique electronic and magnetic properties, which make them promising candidates for carbon-based molecular spintronics. [1-4] The magnetic ordering of these open-shell GNs can be precisely tailored *via* engineering their topological structures and edge configurations. [5,6] In particular, cutting triangular motifs along the zigzag orientation of graphene creates an entire family of triangulenes with high-spin ground states and large spin quantum number scaling linearly with the number of carbon atoms at their zigzag edges. [7-9] The ground-state spin quantum number of the triangulenes is associated with the sublattice imbalance, as predicted by Ovchinnikov's rule and Lieb's theorem for bipartite lattices. [10,11] As such, the ground-state spin quantum number (S) of triangulenes is equal to $\frac{|N_A - N_B|}{2}$, where N_A and N_B represent the number of carbon atoms from the two interpenetrating sublattices (A and B), respectively.

Recently, [3]-, [4]- and [5]triangulene molecules have been successfully fabricated on different surfaces and their chemical structures and spin-polarized edge states have been characterized by scanning probe techniques. [12-14] A further extension of triangulene molecules to a larger system not only increases their ground-state spin quantum number but also offers higher feasibility for the device fabrication. [15] Apart from tuning the size of triangulenes, topological engineering *via* creating an antidot (denoted as antidot engineering) in large triangulene homologues provides an alternative approach to fabricate a series of intriguing triangulene quantum rings (TQRs) with tailored spin quantum number and magnetic ordering associated with both inner and outer zigzag edges. [16-19] Compared to the triangulene counterparts, the presence of an antidot in TQRs results in a larger number of zigzag edges per unit area. Moreover, the spin-polarized energy gap and spin density distribution of TQRs, together with the magnetic ordering in both inner and outer zigzag edges, can be precisely controlled *via* tailoring the topology of antidots. [20-22] Therefore, antidot engineering constitutes a flexible and versatile strategy

towards the fabrication of a plethora of novel magnetic quantum nanostructures, crucial to unlocking their full potential in next-generation spintronics applications.

Analogously to triangulenes, the ground-state spin quantum number of TQRs can also be predicted by Ovchinnikov's rule by evaluating their sublattice imbalance. As illustrated in Figure 1a, excavating a coronene-moiety from the centre of an intact [7]triangulene molecule (Figure 1a, right) generates a [7]TQR molecule containing a hexagonal coronene-like antidot (Figure 1a, middle right). Notably, the as-removed hexagonal motif consists of the equal number of two sublattices (A- and B-type). As a result, the ground-state spin quantum number ($S = 3$) is preserved after introducing such a hexagonal antidot in [7]triangulene. In contrast to [7]triangulene, the presence of inner zigzag edges in [7]TQR is expected to modulate its spin density and magnetic ordering in this system. [21] Similarly, larger TQRs also retain the same high spin quantum after removing hexagonal antidots (e.g., high-order coronene-like moieties) in the triangulene hosts (e.g., [10]TQR, Figure 1b, right). By contrast, incorporating triangular antidots into triangulenes can reduce the sublattice imbalance and thus lower their ground-state spin quantum numbers, as exemplified in the case of [8]TQR and [9]TQR (Figure 1b, left). Both of them have the same ground-state spin quantum number of $S = 3$, lower than that of [8]triangulene ($S = \frac{7}{2}$) and [9]triangulene ($S = 4$), respectively. In this case, the ground-state spin quantum number S only depends on the width of the ring, as defined by the number of benzene units (N_W) between outer and inner edges: $S = 3(N_W + 1)$. [21] Therefore, the ground-state spin quantum number of TQRs can be modulated by tailoring the topology of the antidots, including the lateral size (Figure 1b, right) and width of the ring (Figure 1b, left).

Results and Discussions

To demonstrate the concept of antidot engineering, we designed a new precursor **1** containing a kekulene-core attached by three 2,6-dimethylphenyl substituents at *meso-* positions of three alternating edges. The kekulene is well-known for its annelated macrocyclic topology that provides an ideal platform for antidot engineering. [23-27] The dehydrogenation of methyl groups of precursor **1** generates benzylic

radicals, which then couple with the neighbouring carbon atoms of kekulene-core. Subsequently, an aromaticity-driven ring-closure reaction leads to the formation of [7]TQR (Figure 1a). Precursor **1** was obtained *via* multiple solution-phase synthetic steps as inspired by our previous work (see details in the Supporting Information). [28] In brief, a macrocyclic oligo(*m*-phenylene) intermediates **7** carrying six vinyl ether groups was first synthesized by Suzuki coupling reaction. The subsequent Bi(OTf)$_3$ catalyzed cyclization reaction of **7** in 1,2-dichloroethane at 90 °C led to the formation of the 2,6-dimethylphenyl-substituted kekulene **1** in 76% yield. The structure of the precursor **1** was confirmed by ^{1}H NMR, ^{13}C NMR spectra, and mass spectrum.

Precursor **1** was first deposited onto Au(111) at a submonolayer coverage, under ultra-high vacuum conditions. It exhibits a three-lobed appearance in the STM image attributed to its three-fold structural symmetry (Figure S1). Subsequently, a post-annealing of Au(111) substrate at 550 K for 10 minutes triggers the surface-assisted cyclodehydrogenation of **1** towards the formation of [7]TQR. [29] An overview STM image captures that as-formed products contain both isolated triangular-shaped molecules and irregular oligomers presumably arising from intermolecular coupling on Au(111) during thermal annealing process (Figure 2a, Figure S1). Isolated triangular-shaped molecules constitute approximately 26% of all the products, as estimated by a statistical analysis of multiple STM images. In addition, a magnified STM image of triangular-shaped products with a metallic tip resolves a dim hole-like feature in the molecular centre (Figure 2b and Figure S1) and characteristic edge-localized nodal patterns, resembling the patterns observed at the zigzag edges of the zigzag-edged graphene nanostructures in the previous reports. [13,14,29,30] To probe the chemical structure of an isolated product **1**, we performed bond-resolved STM (BR-STM) imaging with a carbon monoxide-functionalized tip (CO-tip). [31-34] The BR-STM imaging was conducted at constant-height mode with reduced tip-sample distances (i.e. Pauli repulsion regime), wherein the CO molecule undergoes a lateral relaxation over the areas with high electron density (repulsive) areas (chemical bonds), which modulates the overall tunneling conductance between tip and sample, resulting in sharp features associated with the chemical bonds in the current

image. [35,36] The corresponding BR-STM image of a single triangular-shaped molecule (Figure 2c) unambiguously resolves the molecular backbone consisting of twelve fused benzene rings with a clear-cut hexagonal antidot (a diameter of 5.7 Å) in the molecular centre. Furthermore, the flat adsorption geometry of final products on Au(111) indicates the absence of any chemical bonding of molecule to the surface. These observations confirm the successful synthesis of the [7]TQR on Au(111).

To unveil the electronic structure of [7]TQR, we acquired differential conductance spectra ($\mathrm{d}I/\mathrm{d}V$) over a single molecule on Au(111) using a calibrated metallic tip. The characteristic point $\mathrm{d}I/\mathrm{d}V$ spectra collected at the corner (red curve) and the edge centre (blue curve) of a [7]TQR along with the reference spectrum recorded on bare Au(111) (grey dashed curve), are presented in Figure 3a. The $\mathrm{d}I/\mathrm{d}V$ spectrum collected at the edge corner of the molecule (red cross in the inset image in Figure 3a) shows two pronounced peaks at -0.61 V ($\pm$0.05 V) and +0.91 V ($\pm$0.05 V), presumably corresponding to the positive and negative ion resonances (PIR and NIR), respectively. We also observed a weak "bump" feature around -0.3 V ($\pm$0.05 V) that overlaps with the Au(111) surface states, which can be better resolved in $\mathrm{d}I/\mathrm{d}V$ spectrum acquired in a smaller bias range (Figure S3). In addition, a prominent peak at -1.47 V ($\pm$0.05 V) and a substantial rise above +2.0 V can be observed at both $\mathrm{d}I/\mathrm{d}V$ spectra acquired at the corner and the edge centre.

In order to gain a more in-depth insight into the electronic structures of [7]TQR, we performed spin-polarized density functional theory (DFT) calculations. [37,38] Firstly, our calculations reveal that the septuple ground-state ($S = 3$) of a freestanding [7]TQR is lower in energy by 378 and 448 meV than its S=1 open-shell states, respectively (Figure 2d, Figure S2), consistent with the theoretical predictions of the triangulene systems.[13,14] Figure 3b presents the calculated single-particle DFT spin-polarized energy level diagram of a freestanding [7]TQR in the ferromagnetic septuple state ($S = 3$). The frontier orbitals of a neutral [7]TQR (Figure 3a) contain six singly occupied molecular orbitals (denoted as SOMOs including spin-up $\psi_{3\uparrow} - \psi_{8\uparrow}$) and six singly unoccupied molecular orbitals (denoted as SUMOs including spin-down $\psi_{3\downarrow} - \psi_{8\downarrow}$) with the corresponding wave function plots shown in Figure 3d. It is noted that a

large energy splitting of 200 meV between $\psi_{3\uparrow} - \psi_{5\uparrow}$ and $\psi_{6\uparrow} - \psi_{8\uparrow}$ of SOMOs leads to a double peak feature associated to SOMOs in density of states (DOS) (Figure 3c). This is consistent with our experimental observations of a pair of occupied electronic states at -0.61 V and -0.3 V, which thus can be assigned as SOMO$_1$ and SOMO$_2$ (Figure 3c), respectively. In contrast to SOMOs, a reduced energy splitting between SUMOs leads to a single peak feature of SUMOs-derived DOS, in agreement with the experimental observation of a single broad peak located at +0.91 V (labelled as SUMOs in Figure 3c). Such a discrepancy between SOMOs and SUMOs-derived DOS features can be attributed to their different degrees of orbital degeneracy (Figure 3b). According to the energy ordering of these molecular orbitals, a sharp peak at -1.47 V (±0.05 V) and a substantial rise above +2.0 V can be assigned to HOMO-1 (highest occupied molecular orbital) and LUMO+1 (lowest unoccupied molecular orbital) derived from $\psi_{1\downarrow} - \psi_{2\downarrow}$ and $\psi_{9\uparrow} - \psi_{10\uparrow}$, respectively.

To resolve the spatial distribution of these molecular orbitals, we performed the differential conductance mapping at the corresponding energetic positions of the aforementioned peaks (Figure 4a-e). dI/dV maps collected at -0.61 V (Figure 4b), -0.3 V and +0.91 V (Figure 4d) reveal the edge-localization and the characteristic nodal patterns for both the outer and inner edges of [7]TQR, wherein the nodal patterns of outer edges resemble that of π-extended triangulenes in previous reports. [13,14] As for the triangulenes, SOMOs and SUMOs-derived states often show the identical spatial patterns. However, it is noted that dI/dV maps acquired at -0.61 V (SOMO$_1$), -0.30 V (SOMO$_2$), and +0.91 V (SUMOs) exhibit slightly different spatial patterns. Such a difference can be attributed to the different frontier orbitals comprising SOMO$_1$, SOMO$_2$ and SUMOs, respectively. Notably, SOMOs with a lower degree of degeneracy split into two sub-sets of nearly-degenerate orbitals ($\psi_{3\uparrow} - \psi_{5\uparrow}$, SOMO$_1$ and $\psi_{6\uparrow} - \psi_{8\uparrow}$, SOMO$_2$) (Figure 3b and c), resulting in slightly different patterns in the dI/dV maps. All the key features of experimental dI/dV maps taken at -0.61 V and -0.3 V (Figure 4c) are well reproduced in the calculated dI/dV maps involving the orbitals of $\psi_{3\uparrow} - \psi_{5\uparrow}$ (SOMO$_1$) and $\psi_{6\uparrow} - \psi_{8\uparrow}$ (SOMO$_2$). [39] In contrast to SOMOs, SUMOs of [7]TQR with a higher degree of degeneracy (Figure 3b) yield a single

peak in dI/dV spectrum. A direct comparison between experimental and theoretical dI/dV map reveals that orbitals $\psi_{5\downarrow}$ and $\psi_{6\downarrow}$ with similar wave function patterns (Figure 3d) have a considerable contribution (high weightage) to the dI/dV map of SUMOs. Such observations further imply that these probed orbitals, indeed, correspond to the frontier SOMOs and SUMOs of [7]TQR.

In addition, dI/dV map recorded at -1.47 V (HOMO-1) reveals a triangle lobe at the centre and characteristic nodal pattern (three bright lobes) at the outer edges. In contrast, dI/dV map taken at +2.20 V (LUMO+1) exhibits a hexagonal protrusion at the centre and faint feature at the outer edges, suggesting a larger contribution from the inner edge states to LUMO+1. Moreover, the calculated dI/dV images involving the spin-down $\psi_{1\downarrow} - \psi_{2\downarrow}$ and spin-up $\psi_{9\uparrow} - \psi_{10\uparrow}$ orbitals show excellent agreement with dI/dV maps taken at -1.47 V (HOMO-1) and +2.20 V (LUMO+1), respectively (Figure 4f and j).

Lastly, the energy gap of Au-supported [7]TQR is determined to be 1.21 eV based on the energy separation between SOMO$_2$ and SUMOs (Figure 3A), lower than the theoretically predicted value (2.25 eV) of a free-standing [7]TQR. This can be attributed to the gap reduction arising from the screening effect from metallic Au(111) surface, consistent with the observation in π-extended triangulenes and other similar systems. [13,14,40-44] All these observations discussed above manifest that the septuple magnetic ground states ($S = 3$) of [7]TQR is likely to be retained on Au(111).

Conclusion

In summary, we have demonstrated a new synthetic route to use the substituted-kekulene as the precursor for the synthesis of unsubstituted [7]TQR with a coronene-like antidot on Au(111). BR-STM characterization unambiguously reveals the chemical structure of [7]TQR at the sub-molecular level, while dI/dV measurements unveil the spin-polarized electronic states contributed from both inner and outer zigzag edges of [7]TQR. Both experimental data and theoretical calculations suggest that [7]TQR retains its open-shell septuple ground-state ($S = 3$) on Au(111). The successful synthesis of triangulene quantum ring *via* antidot engineering opens up a new avenue for the fabrication of high-spin quantum nanostructures towards next-generation quantum devices.

Conflict of interest

The authors declare no conflict of interest.

Reference

[1]   Y. Morita, S. Suzuki, K. Sato, T. Takui, *Nat. Chem.* **2011**, *3*, 197–204.

[2]   W. Han, R. K. Kawakami, M. Gmitra, J. Fabian, *Nat. Nanotech* **2014**, *9*, 794–807.

[3]   Z. Sun, J. Wu, *J. Mater. Chem.* **2012**, *22*, 4151–4160.

[4]   W. L. Wang, S. Meng, E. Kaxiras, *Nano Lett.* **2008**, *8*, 241–245.

[5]   O. V. Yazyev, *Rep. Prog. Phys.* **2010**, *73*, 056501–17.

[6]   S. Fujii, T. Enoki, *Acc. Chem. Res.* **2013**, *46*, 2202–2210.

[7]   J. Fernández-Rossier, J. J. Palacios, *Phys. Rev. Lett.* **2007**, *99*, 177204–4.

[8]   A. D. Güçlü, P. Potasz, P. Hawrylak, *Phys. Rev. B* **2013**, *88*, 155429–8.

[9]   W. L. Wang, O. V. Yazyev, S. Meng, E. Kaxiras, *Phys. Rev. Lett.* **2009**, *102*, 195–4.

[10]   A. A. Ovchinnikov, *Theoret. Chim. Acta* **1978**, *47*, 297–304.

[11]   E. Lieb, *Phys. Rev. Lett.* **1989**, *62*, 1201–1204.

[12]   N. Pavliček, A. Mistry, Z. Majzik, N. Moll, G. Meyer, D. J. Fox, L. Gross, *Nat. Nanotech* **2017**, *12*, 308–311.

[13]   S. Mishra, D. Beyer, K. Eimre, J. Liu, R. Berger, O. Gröning, C. A. Pignedoli, K. Müllen, R. Fasel, X. Feng, P. Ruffieux, *J. Am. Chem. Soc.* **2019**, *141*, 10621–10625.

[14]   J. Su, M. Telychko, P. Hu, G. Macam, P. Mutombo, H. Zhang, Y. Bao, F. Cheng, Z.-Q. Huang, Z. Qiu, S. J. R. Tan, H. Lin, P. Jelínek, F.-C. Chuang, J. Wu, J. Lu, *Sci. Adv.* **2019**, *5*, eaav7717–7.

[15]   J. Su, M. Telychko, S. Song, J. Lu, *Angew. Chem. Int. Ed.* **2020**, *75*, 2667–13.

[16]   H.-X. Yang, M. Chshiev, D. W. Boukhvalov, X. Waintal, S. Roche, *Phys. Rev. B* **2011**, *84*, 214404–7.

[17]   T. G. Pedersen, C. Flindt, J. Pedersen, N. A. Mortensen, A.-P. Jauho, K. Pedersen, *Phys. Rev. Lett.* **2008**, *100*, 136804–4.

[18]   R. Pawlak, X. Liu, S. Ninova, P. D'Astolfo, C. Drechsel, S. Sangtarash, R. Häner, S. Decurtins, H. Sadeghi, C. J. Lambert, U. Aschauer, S.-X, Liu, E. Meyer, *J. Am. Chem. Soc.* **2020**, *142*, 12568–12573.

[19]   C. Moreno, M. Vilas-Varela, B. Kretz, A. García-Lekue, M. V. Costache, M. Paradinas, M. Panighel, G. Ceballos, S. O. Valenzuela, D. Peña, A. Mugarza, *Science* **2018**, *360*, 199–203.

[20]   D. A. Bahamon, A. L. C. Pereira, P. A. Schulz, *Phys. Rev. B* **2009**, *79*, 125414–7.

[21]   P. Potasz, A. D. Güçlü, O. Voznyy, J. A. Folk, P. Hawrylak, *Phys. Rev. B* **2011**, *83*, 174441–6.

[22]   M. Grujić, M. Tadić, F. M. Peeters, *Phys. Rev. B* **2013**, *87*, 085434–6.

[23]   H. A. Staab, F. Diederich, *Chem. Ber.* **1983**, *116*, 3487–3503.

[24]   J. C. Buttrick, B. T. King, *Chem. Soc. Rev.* **2017**, *46*, 7–20.

[25]   I. Pozo, Z. Majzik, N. Pavliček, M. Melle-Franco, E. Guitián, D. Peña, L. Gross, D. Pérez, *J. Am. Chem. Soc.* **2019**, *141*, 15488–15493.

[26]   M. Di Giovannantonio, X. Yao, K. Eimre, J. I. Urgel, P. Ruffieux, C. A. Pignedoli, K. Müllen, R. Fasel, A. Narita, *J. Am. Chem. Soc.* **2020**, *142*, 12046–12050.

[27]   Q. Fan, D. Martin-Jimenez, S. Werner, D. Ebeling, T. Koehler, T. Vollgraff, J. Sundermeyer, W. Hieringer, A. Schirmeisen, J. M. Gottfried, *J. Am. Chem. Soc.* **2020**, *142*, 894–899.

[28]   W. Fan, Y. Han, S. Dong, G. Li, X. Lu, J. Wu, *CCS Chem.* **2020**, 1445–1452.

[29]   P. Ruffieux, S. Wang, B. Yang, C. Sánchez-Sánchez, J. Liu, T. Dienel, L. Talirz, P. Shinde, C. A. Pignedoli, D. Passerone, T. Dumslaff, X. Feng, K. Müllen, R. Fasel, *Nature* **2016**, *531*, 489–492.

[30]   L. Talirz, H. Söde, J. Cai, P. Ruffieux, S. Blankenburg, R. Jafaar, R. Berger, X. Feng, K. Müllen, D. Passerone, R. Fasel, C. A. Pignedoli, *J. Am. Chem. Soc.* **2013**, *135*, 2060–2063.

[31]   G. D. Nguyen, H.-Z. Tsai, A. A. Omrani, T. Marangoni, M. Wu, D. J. Rizzo, G. F. Rodgers, R. R. Cloke, R. A. Durr, Y. Sakai, F. Liou, A. S. Aikawa, J. R. Chelikowsky, S. Louie, F. Fischer, M. F. Crommie, *Nat. Nanotech.* **2017**, *12*, 1077–1082.

[32]   J. Li, N. Merino-Díez, E. Carbonell-Sanromà, M. Vilas-Varela, D. G. de Oteyza, D. Peña, M. Corso, J. I. Pascual, *Sci. Adv.* **2018**, *4*, eaaq0582–7.

[33]   J. Li, S. Sanz, J. Castro-Esteban, M. Vilas-Varela, N. Friedrich, T. Frederiksen, D. Peña, J. I. Pascual, *Phys. Rev. Lett.* **2020**, *124*, 177201.

[34]   S. Song, N. Guo, X. Li, G. Li, Y. Haketa, M. Telychko, J. Su, P. Lyu, Z. Qiu, H. Fang, X. Peng, J. Li, X. Wu, Y. Li, C. Su, M. J. Koh, J. Wu, H. Maeda, C. Zhang, J. Lu, *J. Am. Chem. Soc.* **2020**, *142*, 13550–13557.

[35]   P. Hapala, G. Kichin, C. Wagner, F. S. Tautz, R. Temirov, P. Jelínek, *Phys. Rev. B* **2014**, *90*, 1989–9.

[36]   P. Hapala, R. Temirov, F. S. Tautz, P. Jelínek, *Phys. Rev. Lett.* **2014**, *113*, 226101–5.

[37]   V. Blum, R. Gehrke, F. Hanke, P. Havu, V. Havu, X. Ren, K. Reuter, M. Scheffler, *Computer Physics Communications* **2009**, *180*, 2175–2196.

[38]   J. P. Perdew, M. Ernzerhof, K. Burke, *J. Chem. Phys.* **1996**, *105*, 9982–9985.

[39]   O. Krejčí, P. Hapala, M. Ondráček, P. Jelínek, *Phys. Rev. B* **2017**, *95*, 045407–9.

[40]   P. Ruffieux, J. Cai, N. C. Plumb, L. Patthey, D. Prezzi, A. Ferretti, E. Molinari, X. Feng, K. Müllen, C. A. Pignedoli, R. Fasel, *ACS Nano* **2012**, *6*, 6930–6935.

[41]   Y. J. Zheng, Y. L. Huang, Y. Chen, W. Zhao, G. Eda, C. D. Spataru, W. Zhang, Y.-H. Chang, L.-J. Li, D. Chi, S. Y. Quek, A. T. S. Wee, *ACS Nano* **2016**, *10*, 2476–2484.

[42]   J. B. Neaton, M. S. Hybertsen, S. G. Louie, *Phys. Rev. Lett.* **2006**, *97*, 98–4.

[43]   Z.-F. Liu, D. A. Egger, S. Refaely-Abramson, L. Kronik, J. B. Neaton, *J. Chem. Phys.* **2017**, *146*, 092326–14.

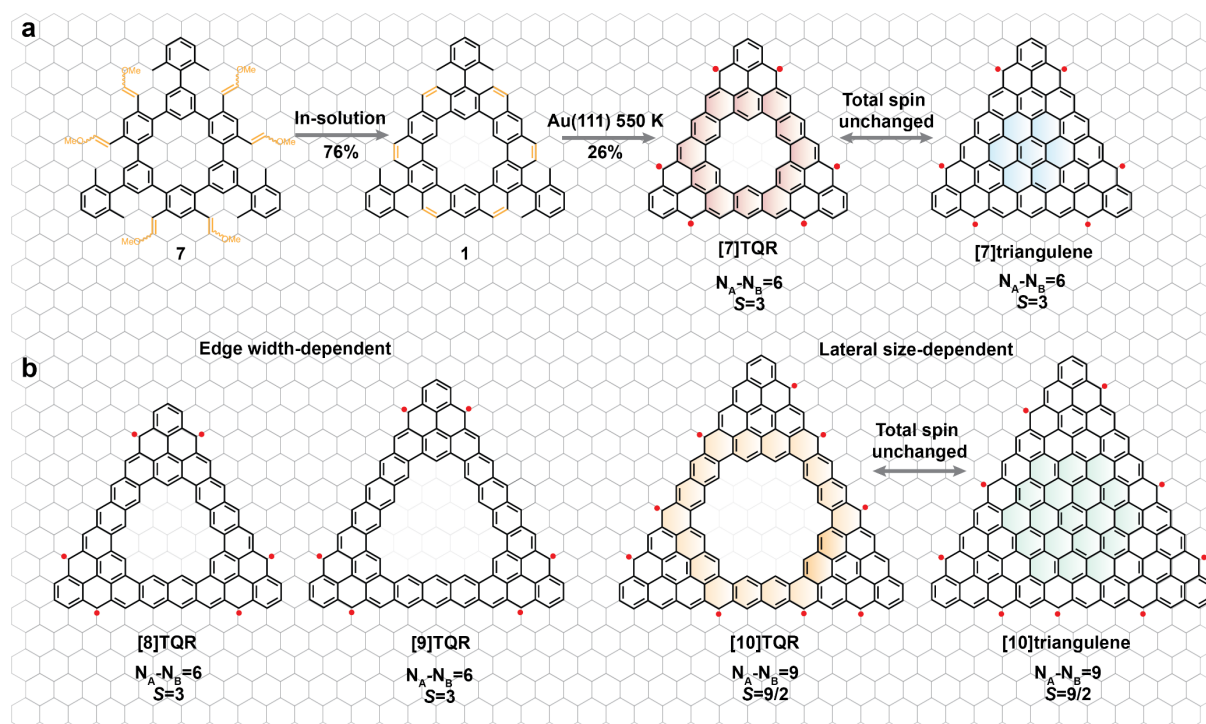[44]   K. S. Thygesen, A. Rubio, *Phys. Rev. Lett.* **2009**, *102*, 046802–4.

Figure 1. Schematic illustration of the synthesis of [7]TQR *via* antidot engineering of triangulene molecules. (a) Illustration of the synthetic route towards [7]TQR. [7]TQR with a coronene-like antidot and [7]triangulene have the same ground-state quantum spin number of $S = 3$. (b) Engineering of triangular and hexagonal antidots within π-extended triangulene molecules. Incorporating a triangular antidot in the centre of triangulene modifies the molecules' ground-state spin quantum number. In contrast, introducing a hexagonal antidot in both [7] and [10]- triangulene retains the ground-state spin quantum number
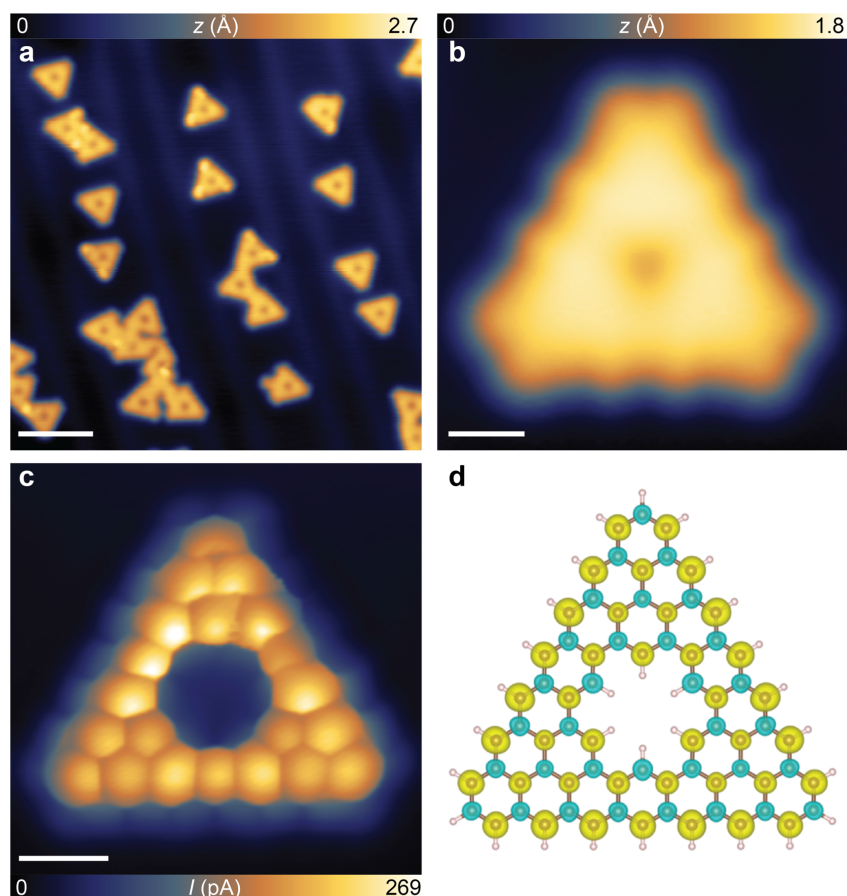
Figure 2. Structural characterization of a single [7]TQR synthesized on Au(111). (a) Large-scale STM image of [7]TQR molecules on Au(111) after annealing the precursor **1** at 550 K (V=1.0 V, I=300 pA). (b) Magnified high-resolution STM image of an individual [7]TQR molecule (V=-0.61 V, I=600 pA). (c) Corresponding BR-STM image (V= 5 mV, Δz= -1.1 Å, setpoint prior to turn off feedback: V=50 mV, I=300 pA). (d) DFT-calculated spin density distribution of a freestanding [7]TQR molecule. Scale bar: a: 4 nm, b and c: 5 Å.
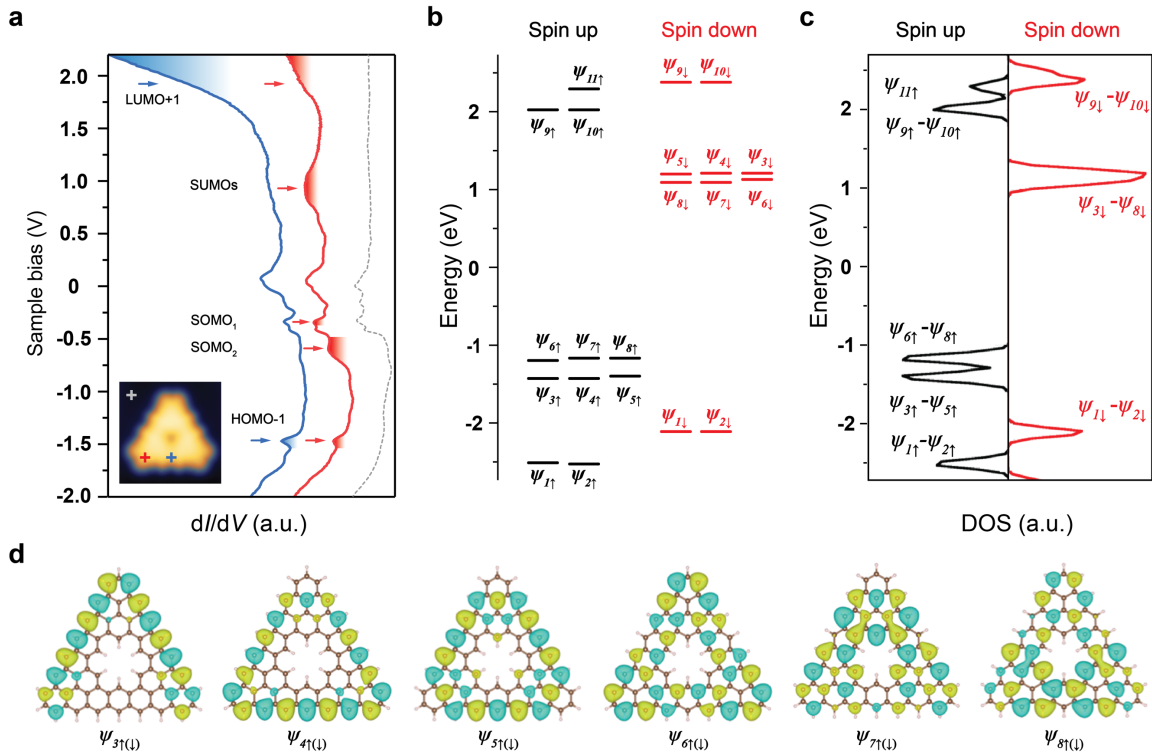
Figure 3. Electronic structure characterization of 7TQR. (a) Point dI/dV spectra acquired over different sites of [7]TQR and Au(111) substrate. dI/dV curves taken at the corner (red curve), centre of the edge (blue curve) and taken on Au(111) (grey-dashed curve). (b) DFT-calculated spin-polarized molecular orbital energy diagram of a freestanding [7]TQR. The black and red symbols refer to spin-up and spin-down states, respectively. (c) Calculated density of states (DOS) of a freestanding [7]TQR. (d) DFT calculated wave functions of six pairs of SOMOs and SUMOs ($\psi_{3\uparrow\downarrow} - \psi_{8\uparrow\downarrow}$). The blue and green isosurface colours indicate opposite phase of the wave function, respectively. (a.u., arbitrary units).
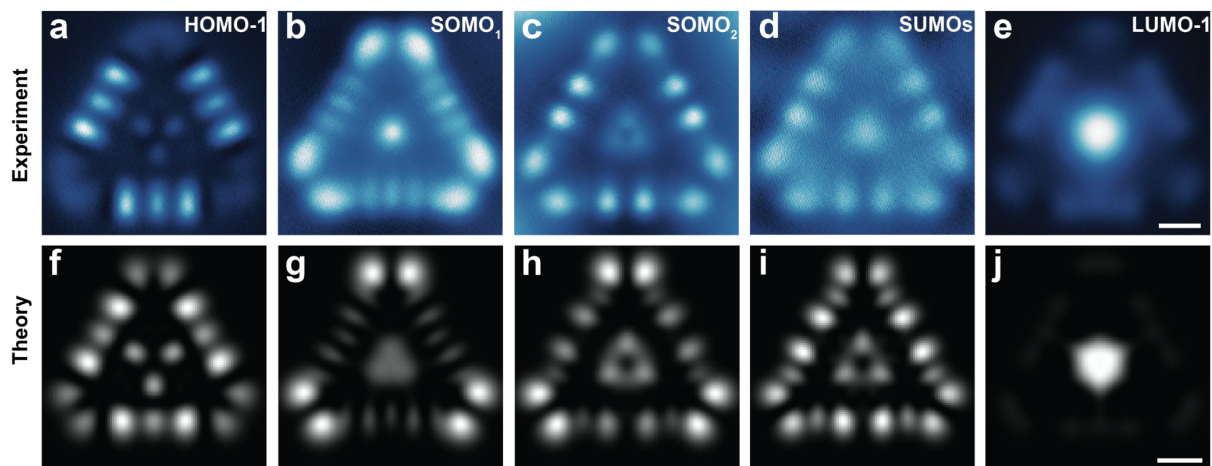
Figure 4. Experimental and calculated dI/dV maps of 7TQR. (a)- (e) Constant-current dI/dV maps recorded at different energy positions. (a) and (e) refer to the HOMO-1 (-1.47 V) and LUMO+1 (+2.20 V), of [7]TQR respectively. (b-d) and refer to the SOMO$_1$ (-0.61 V), SOMO$_2$ (-0.3 V) and SUMOs (+0.91 V) of 7TQR, respectively. (f)-(j) Simulated dI/dV maps acquired at different energy positions corresponding to different sets of orbitals: (f) $\psi_{1\downarrow} - \psi_{2\downarrow}$, (g) $\psi_{3\uparrow} - \psi_{5\uparrow}$, (h) $\psi_{6\uparrow} - \psi_{8\uparrow}$, (i) $\psi_{3\downarrow} - \psi_{8\downarrow}$ and (j) $\psi_{9\uparrow} - \psi_{10\uparrow}$. Scale bar: 5 Å.